

Terrain estimation for high-speed rough-terrain autonomous vehicle navigation

Karl Iagnemma*, Steven Dubowsky

Department of Mechanical Engineering, Massachusetts Institute of Technology
Cambridge, MA 02139 USA

ABSTRACT

High-speed unmanned ground vehicles have important potential applications, including reconnaissance, material transport, and planetary exploration. During high-speed operation, it is important for a vehicle to sense changing terrain conditions, and modify its control strategies to ensure aggressive, yet safe, operation. In this paper, a framework for terrain characterization and identification is briefly described, composed of 1) vision-based classification of upcoming terrain, 2) terrain parameter identification via wheel-terrain interaction analysis, and 3) terrain classification based on auditory wheel-terrain contact signatures. The parameter identification algorithm is presented in detail. The algorithm derives from simplified forms of classical terramechanics equations. An on-line estimator is developed to allow rapid identification of critical terrain parameters. Simulation and experimental results show that the terrain estimation algorithm can accurately and efficiently identify key terrain parameters for sand.

Keywords: Mobile robots, control, terramechanics, high-speed, rough terrain

1. INTRODUCTION

Unmanned ground vehicles (UGVs) have important potential applications, such as reconnaissance, patrol, material transport, and planetary exploration [4, 12, 14] (see Figure 1). Most current UGVs move slowly and conservatively, limiting their effectiveness. At high speeds, vehicle-terrain interaction and vehicle dynamics strongly influence a vehicle's mobility. Thus, control and motion planning algorithms based on physical models of the vehicle and terrain are required to ensure aggressive, yet safe, high-speed operation of a UGV. Also, these models must be updated on-line, to adapt to changing UGV and terrain conditions. A concept of a high-speed UGV is shown in Figure 2.



Figure 1: DEMO III XUV unmanned ground vehicle

Although numerous researchers have studied vehicle modeling, few have studied on-line terrain classification and identification. Here, we define terrain classification as the grouping of terrain regions into pre-defined classes, such as loose soil, muskeg, rock, etc. We define terrain identification as estimation of terrain physical parameters, such as

*kdi@mit.edu; phone (617) 253 5095, Room 3-472M, 77 Massachusetts Avenue, Cambridge MA, 02139 USA

cohesion, internal friction angle, shear deformation modulus, etc. Terrain classification and identification allow a vehicle to detect changing terrain conditions, and adapt its control and motion planning algorithms. Without terrain classification and identification, a UGV must perform conservatively and travel at reduced speeds to avoid failure.



Figure 2: High-speed unmanned ground vehicle concept

One recent study in terrain classification utilized vision-based segmentation of natural terrain into soil and vegetation, with promising results [3]. Visual cues such as color, geometric shape, and texture can all be used to aid classification. No literature exists in the area of terrain classification via non-vision based sensors, such as auditory or thermal sensors. These types of sensors are potential low-cost, low-complexity complements to vision-based sensors.

Terrain identification has received significant attention over the past forty years [1, 2, 11]. However, most reported methods rely on costly, dedicated equipment and require off-line analysis [9, 13]. Few researchers have addressed the problem of on-line terrain identification. In one interesting application, parameter estimation of Martian soil has been performed by the Sojourner rover [8]. The Sojourner rover used the rover wheel as a bevameter-type device to identify soil cohesion and internal friction angle. However, it used off-line analysis techniques to compute soil parameters.

In this paper we briefly describe a framework for terrain characterization and identification. The framework is composed of 1) vision-based classification of upcoming terrain, 2) terrain parameter identification via wheel-terrain interaction analysis, and 3) terrain classification based on the auditory wheel-terrain contact signature. This paper then describes in detail the parameter identification algorithm. The algorithm is based on simplified forms of classical terramechanics equations, and uses a linear-least squares estimator to compute terrain parameters in real time. The method is computationally efficient, and is thus suitable for implementation on a vehicle with limited on-board computational resources. Simulation and experimental results show that the terrain estimation algorithm can accurately and efficiently identify key terrain parameters for sand.

2. TERRAIN CHARACTERIZATION AND IDENTIFICATION SYSTEM DESCRIPTION

The intended scenario is one in which a UGV performs short, high-speed traverses interspersed with periodic slower traverses. Visual and auditory terrain classification is performed during both high-speed and low-speed traverses. Terrain parameter identification is performed only during low-speed traverses, due to requirements inherent in the estimation algorithm.

Each of these methods allow a UGV to detect changing terrain conditions. In an example scenario, a UGV visually classifies an upcoming terrain region as loose sand, and assumes a nominal cohesion and internal friction angle for feedback into its motion planning and control algorithms. As the UGV traverses the terrain region, the cohesion and internal friction angle are identified through the terrain identification algorithm. This information is then associated with the “loose sand” terrain class. As the UGV travels, a terrain information database is compiled, which can be used for predictive motion planning and advanced feedback control schemes, and allow more aggressive mobility behavior (see

Figure 4) [6, 7]. Thus, the vehicle performs low-speed tests to enable high-speed behavior. Terrain parameters learned at low-speed are coupled with classification cues observed at high-speed.

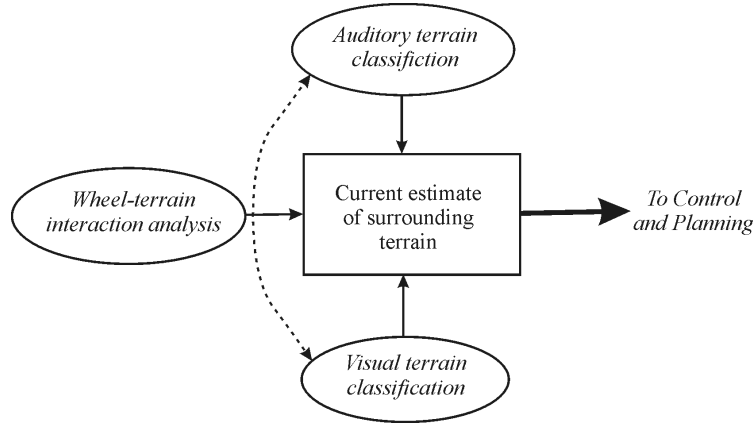


Figure 3: Terrain characterization and identification diagram

Note that visual and auditory classification systems supply redundant information. In situations where high quality image information is not available (due to motion blur, for example), the auditory sensor can be used. In situations where high quality auditory information is not available (during situations with high-volume noise disturbances, for example), vision information can be used. In situations where both systems are supplying high quality information, the information is fused.

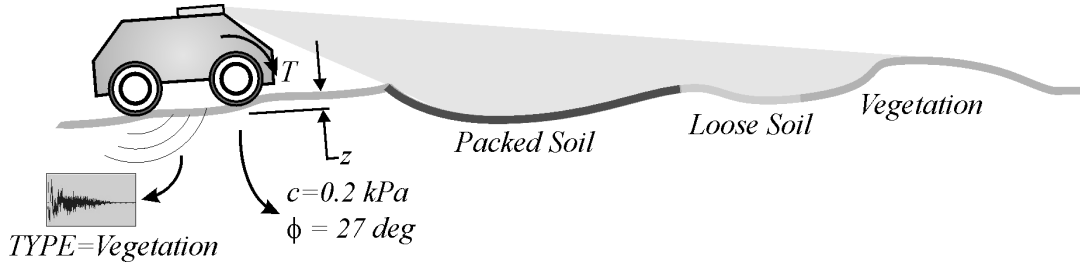


Figure 4: UGV Performing terrain characterization and identification

Vision and auditory terrain classification are current research activities in our laboratory. The remainder of this paper presents a method for low-speed terrain parameter identification.

3. TERRAIN PARAMETER IDENTIFICATION

The purpose of terrain parameter identification is to estimate key terrain parameters on-line, using on-board vehicle sensors. Two key terrain parameters are the cohesion, c , and internal friction angle, ϕ . These parameters can be used to compute the terrain shear strength, and thus give an estimate of vehicle traversability, from Coulomb's equation:

$$\tau_{\max} = (c + \sigma_{\max} \tan \phi) \tag{1}$$

where σ is the normal stress acting on the terrain region.

Here, the case of a rigid wheel traveling through deformable terrain is considered. Note that this is a commonly occurring case, since the stiffness of an inflated pneumatic tire is often rigid compared to natural terrain [1].

To estimate terrain physical parameters, equations relating the parameters of interest to physically measurable quantities must be developed. A free-body diagram of a driven rigid wheel traveling through deformable terrain is shown in Figure

5. A vertical load W and a horizontal force DP are applied to the wheel by the vehicle suspension. A torque T is applied at the wheel rotation axis by an actuator. The wheel has angular velocity ω , and the wheel center possesses a linear velocity, V . The angle from the vertical at which the wheel first makes contact with the terrain is denoted θ_1 . The angle from the vertical at which the wheel loses contact with the terrain is denoted θ_2 . Thus, the entire angular wheel-terrain contact region is defined by $\theta_1 + \theta_2$.

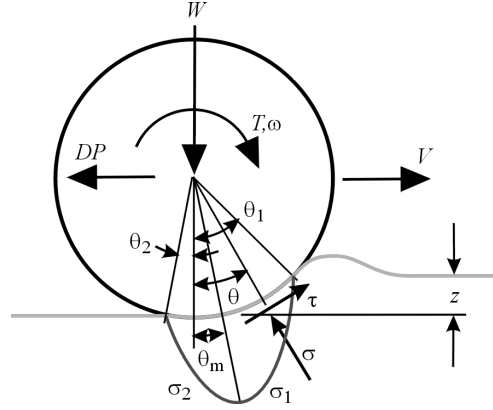


Figure 5: Free-body diagram of rigid wheel on deformable terrain

A stress region is created at the wheel-terrain interface, as indicated by the regions σ_1 and σ_2 . At a given point on the interface, the stress can be decomposed into a component acting normal to the wheel at the wheel-terrain contact point, σ , and a component acting parallel to the wheel at the wheel-terrain contact point, τ . The angle from the vertical at which the maximum stress occurs is denoted θ_m .

In the following analysis it is assumed that the following quantities are known: the vertical load W , torque T , sinkage z , wheel angular speed ω , and wheel linear speed V . The vertical load W can be computed from a quasi-static analysis of the vehicle, with knowledge of the mass distribution. Static analysis is valid due to the assumption that the vehicle will be traveling at low speeds [14]. The torque T can be estimated with reasonable accuracy from the current input to an electrical drive motor, or by instrumenting the wheel axle with force sensors. The sinkage z can be computed from kinematic analysis of the vehicle, or via fused vision-odometry techniques [8, 15]. The wheel angular speed ω can be measured with a tachometer. The wheel linear speed V can be computed using IMU measurements, or vision-based scene analysis techniques [5]. Thus, all required inputs can be measured or estimated with on-board sensors.

Force balance equations are written for the system in Figure 5, as:

$$W = rb \left(\int_{\theta_1}^{\theta_2} \sigma(\theta) \cos \theta \cdot d\theta + \int_{\theta_1}^{\theta_2} \tau(\theta) \sin \theta \cdot d\theta \right) \quad (2)$$

$$DP = rb \left(\int_{\theta_1}^{\theta_2} \tau(\theta) \cos \theta \cdot d\theta - \int_{\theta_1}^{\theta_2} \sigma(\theta) \sin \theta \cdot d\theta \right) \quad (3)$$

$$T = r^2 b \int_{\theta_1}^{\theta_2} \tau(\theta) \cdot d\theta \quad (4)$$

The shear stress is described as:

$$\tau(\theta) = (c + \sigma(\theta) \tan \phi) \left(1 - e^{-\frac{r}{k} [\theta_1 - \theta - (1-i)(\sin \theta_1 - \sin \theta)]} \right) \quad (5)$$

where k is the shear deformation modulus, r is the wheel radius, and i is the wheel slip, defined as $i = 1 - (V/r\omega)$ [10, 16].

The normal stress at the wheel-terrain interface is given by:

$$\sigma(z) = (k_1 + k_2 b) \left(\frac{z}{b} \right)^n \quad (6)$$

where b is the wheel width, k_1 and k_2 are constants, and n is the sinkage coefficient [1]. An expression for the normal stress as a function of the wheel angular location θ is written by expressing the sinkage as a function of the angular location θ :

$$z(\theta) = r(\cos\theta - \cos\theta_1) \quad (7)$$

Substituting Equation (7) into Equation (6) yields expressions for the normal stress distribution along the wheel-terrain interface, as:

$$\sigma_1(\theta) = (k_1 + k_2 b) \left(\frac{r}{b} \right)^n (\cos\theta - \cos\theta_1)^n \quad (8)$$

$$\sigma_2(\theta) = (k_1 + k_2 b) \left(\frac{r}{b} \right)^n \left(\cos \left(\theta_1 - \frac{\theta}{\theta_m} (\theta_1 - \theta_m) \right) - \cos\theta_1 \right)^n \quad (9)$$

Analytical expressions for the force balance equations (Equations (2-4)) are required to estimate the cohesion and internal friction angle. However, Equations (2-4) are not amenable to symbolic manipulation, due to their complexity. This complexity motivates the use of an approximate form of the stress equations.

3.1 Equation simplification

Figure 6 is a plot of the shear and normal stress distributions (as defined by Equations (5) and (8-9), respectively) around the rim of a driven rigid wheel on deformable terrain for a range of slip, i , and sinkage coefficient, n . Note that although numerous parameters influence the shape of the stress distribution curves, n and i dominate, and are thus the primary parameters of interest.

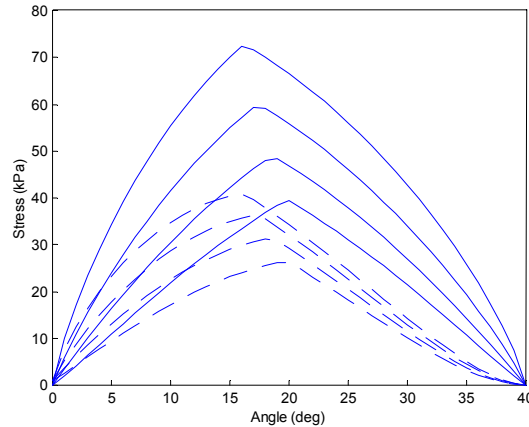


Figure 6: Normal stress (solid) and shear stress (dashed) distribution for varying slip and sinkage

The shear and normal stress distribution curves are approximately triangular for a wide range of parameters. Based on this observation, a linear approximation of the shear and normal stress distribution equations can be written as:

$$\sigma_1(\theta) = \frac{\theta_1 - \theta}{\theta_1 - \theta_m} \sigma_m \quad (10)$$

$$\sigma_2(\theta) = \frac{\theta}{\theta_m} \sigma_m \quad (11)$$

$$\tau_1(\theta) = \frac{\theta_1 - \theta}{\theta_1 - \theta_m} \tau_m \quad (12)$$

$$\tau_2(\theta) = \frac{\theta}{\theta_m} \tau_m \quad (13)$$

where σ_m and τ_m are the maximum values of the normal and shear stress, respectively.

Simulations were conducted to compare the linear approximations (Equations (10-13)) to the original nonlinear equations (Equations (5, 8-9)). Approximately 60,000 simulations were conducted in the following parameter space: $20.0 < \theta_l$ (deg) < 60.0 , $0.6 < n < 1.2$, $20.0 < \phi$ (deg) < 40.0 , $0.0 < c$ (kPa) < 3.0 , $0.0 < k_l$ (kPa) < 140.0 , $520.0 < k_2$ (kN/m³) < 680.0 , $0.005 < k$ (m) < 0.04 , $0.0 < i < 1.0$. The simulated wheel radius r was 0.25 m, and the width b was 0.2 m. These parameter ranges are reasonable for a small vehicle traveling on soft, deformable terrain.

An average difference of 9.34% was found between the approximate and actual normal stress distribution equations, and 12.15% between the approximate and actual shear stress distribution equations. Thus, the linear approximations were considered sufficiently accurate representations of the true nonlinear functions.

Simplified forms of the force balance equations can now be written by combining Equations (2-4) and Equations (10-13), as:

$$W = rb \left(\begin{array}{l} \int_0^{\theta_m} \sigma_2(\theta) \cos \theta \cdot d\theta + \int_{\theta_m}^{\theta_1} \sigma_1(\theta) \cos \theta \cdot d\theta \\ + \int_0^{\theta_m} \tau_2(\theta) \sin \theta \cdot d\theta + \int_{\theta_m}^{\theta_1} \tau_1(\theta) \sin \theta \cdot d\theta \end{array} \right) \quad (14)$$

$$DP = rb \left(\begin{array}{l} \int_0^{\theta_m} \tau_2(\theta) \cos \theta \cdot d\theta + \int_{\theta_m}^{\theta_1} \tau_1(\theta) \cos \theta \cdot d\theta \\ - \int_0^{\theta_m} \sigma_2(\theta) \sin \theta \cdot d\theta - \int_{\theta_m}^{\theta_1} \sigma_1(\theta) \sin \theta \cdot d\theta \end{array} \right) \quad (15)$$

$$T = r^2 b \left(\int_0^{\theta_m} \tau_2(\theta) \cdot d\theta + \int_{\theta_m}^{\theta_1} \tau_1(\theta) \cdot d\theta \right) \quad (16)$$

Evaluation of Equations (14) and (16) leads to the following expressions for the normal load and torque:

$$W = \frac{rb}{\theta_m (\theta_1 - \theta_m)} \left[\sigma_m (\theta_1 \cos \theta_m - \theta_m \cos \theta_1 - \theta_1 + \theta_m) + \tau_m (\theta_1 \sin \theta_m - \theta_m \sin \theta_1) \right] \quad (17)$$

$$T = \frac{1}{2} r^2 b \tau_m \theta_1 \quad (18)$$

Two assumptions are made in solving Equations (17) and (18). The first is that the location of the maximum shear and normal stress occur at the same location θ_m . Analysis and simulation has shown that this assumption is reasonable for a wide range of soil values. With this assumption, an additional relation can be written, based on Equation (5):

$$\tau_m = (c + \sigma_m \tan \phi) \left(1 - e^{-\frac{r}{k}[\theta_1 - \theta_m - (1-i)(\sin \theta_1 - \sin \theta_m)]} \right) \quad (19)$$

The second assumption is that the angular location of maximum stress, θ_m , occurs midway between θ_1 and θ_2 , i.e. $\theta_m = (\theta_1 + \theta_2) / 2$. Analysis and simulation has shown that this assumption is reasonable for a wide range of soils with low to moderate slip ratios.

The system of Equations (17-19) can be combined into a single equation relating the cohesion and internal friction angle (with $\theta_2 = 0$), as:

$$c = \frac{\left(\left(4T \sin(\theta_1) + W\theta_1^2 r - 8T \sin\left(\frac{\theta_1}{2}\right) \right) \tan(\phi) + \left(4T \cos(\theta_1) - 8T \cos\left(\frac{\theta_1}{2}\right) + 4T \right) / (1 - A_1) \right)}{2r^2 w \theta_1 \left(\cos(\theta_1) - 2 \cos\left(\frac{\theta_1}{2}\right) + 1 \right)} \quad (20)$$

where $A_1 = e^{-\frac{r}{k}\left(\frac{\theta_1}{2} + (1-i)\left(-\sin(\theta_1) + \sin\left(\frac{\theta_1}{2}\right)\right)\right)}$.

Equation (20) is a single equation in two unknowns. During the parameter estimation process, sensor data is recorded at each sampling point j . Thus, for a vehicle moving at low speed with a reasonable sampling rate (i.e. several hertz), numerous data points can be collected within a small terrain region. Equation (20) can then be written j times, and solved in a least-squares fashion, as:

$$\mathbf{K}_1 = \mathbf{K}_2 \begin{bmatrix} c \\ \tan \phi \end{bmatrix} \quad (21)$$

$$\begin{bmatrix} c \\ \tan \phi \end{bmatrix} = (\mathbf{K}_2^T \mathbf{K}_2)^{-1} \mathbf{K}_2^T \mathbf{K}_1 \quad (22)$$

with $\mathbf{K}_1 = [K_{11} \ K_{12} \ \dots \ K_{1j}]^T$, $\mathbf{K}_2 = [\mathbf{K}_{21} \ \mathbf{K}_{22} \ \dots \ \mathbf{K}_{2j}]^T$, and

$$K_1 = \left(4T \cos(\theta_1) - 8T \cos\left(\frac{\theta_1}{2}\right) + 4T \right) / (1 - A_1)$$

$$\mathbf{K}_2 = \begin{bmatrix} 2r^2 w \theta_1 \left(\cos(\theta_1) - 2 \cos\left(\frac{\theta_1}{2}\right) + 1 \right) \\ - \left(4T \sin(\theta_1) + W\theta_1^2 r - 8T \sin\left(\frac{\theta_1}{2}\right) \right) \end{bmatrix}^T$$

All quantities in Equation (22) can be sensed except the shear deformation modulus k . However, the estimation process exhibits low sensitivity to error in k , and thus k is chosen as a representative value for deformable terrain.

4. SIMULATION RESULTS

Simulations were conducted in Matlab of a single driven wheel traveling through deformable terrain. The purpose of the simulation was to examine the accuracy of the parameter estimation algorithm in the presence of noisy and uncertain inputs.

The wheel was commanded to travel at approximately 5 cm/sec. The simulated sensor inputs W , T , z , and i were corrupted with white noise of a magnitude equivalent to 10% of their maximum value. The simulated sampling rate was 10 Hz. The shear deformation modulus k was assumed to be 300% of its actual value.

The following parameter set was used: $r = 0.5$ m, $w = 0.3$ m, $k = 0.005$ m, $k_1 = 20.0$ kPa, $k_2 = 600$ kN/m³, $n = 0.9$. The cohesion and internal friction angle were $c = 1.0$ kPa, $\phi = 30.0$.

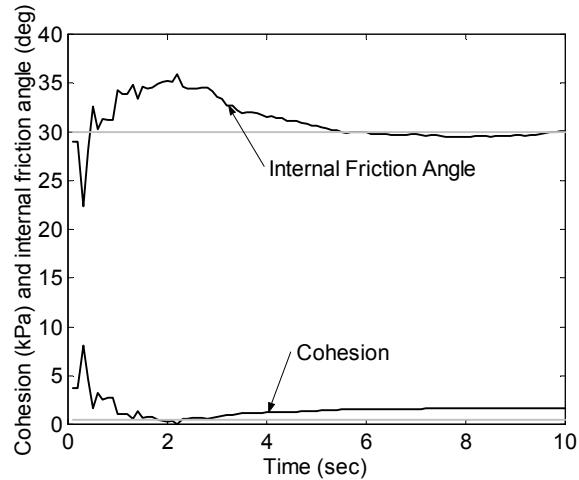


Figure 7: Simulated comparison of estimated cohesion (black) and internal friction angle (black) to true values (gray)

A representative result is shown in Figure 7. It can be seen that the estimated parameters rapidly approach their true values. Small differences remain, due to the simplifying assumptions in the estimation process. However, it can be seen that the estimation algorithm produces accurate results. The computational load for the algorithm is approximately 2-3 msec per estimation cycle for unoptimized Matlab code.

The simplifying assumptions also allow prediction of the drawbar pull (Equation (15)) using only sensed inputs. The drawbar pull is a measure of the net forward force created by the wheel, and is thus an important part of traversability prediction. Figure 8 shows a comparison of the actual and predicted drawbar pull for the simulation run described above. The predicted drawbar pull is very close to the actual value.

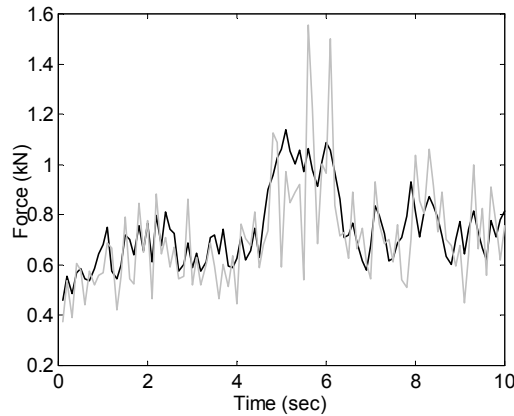


Figure 8: Actual (black) and predicted (gray) drawbar pull

5. EXPERIMENTAL RESULTS

Experiments were performed on the Field and Space Robotics Laboratory terrain characterization testbed, shown in Figure 9. The testbed consists of a driven rigid wheel mounted on an undriven vertical axis. The wheel assembly is mounted to a driven horizontal carriage. By driving the wheel and carriage at different rates, variable slip ratios can be imposed. The vertical wheel load can be changed by adding weight to the vertical axis.

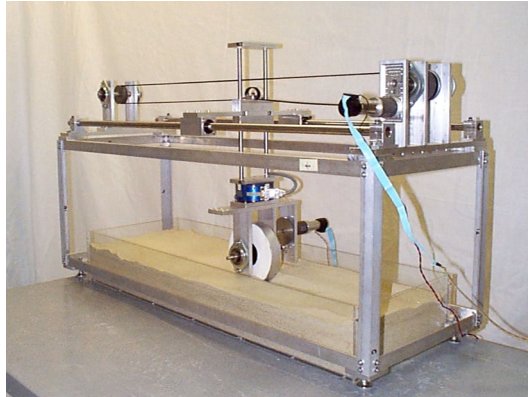


Figure 9: Field and Space Robotics Laboratory terrain characterization testbed

The testbed is instrumented with encoders to measure angular velocities of both the wheel and the carriage pulley. The carriage linear velocity is computed from the carriage pulley angular velocity. The vertical wheel sinkage is measured with a linear potentiometer. The current input to the wheel is estimated by measuring the voltage across a current-sense resistor. The six-component wrench between the wheel and carriage is measured with an AMTI six-axis force/torque sensor. The force sensor allows measurement of the normal load W and drawbar pull DP . The estimation algorithm is run on an Intel 486 66 Mhz processor at a rate of 250 Hz.

The wheel diameter and width are 14.6 and 6.0 cm., respectively. The wheel maximum angular velocity is 1.1 rad/sec. This results in a maximum linear velocity of 8.0 cm/sec, which is identical to the maximum carriage velocity.

Terrain parameter identification experiments were run in sand. Results of a representative experiment are shown in Figure 10. The estimation algorithm gives parameter estimates for c and ϕ in the range of -3.1 - 2.2 kPa and 26° - 43° , respectively. (Note that estimated negative values for cohesion are not physically meaningful.) Published data for c and ϕ for loose sand falls in a range between 0 - 1.0 kPa and 25° - 32° , respectively [1]. Experiments to characterize loose sand with a bevameter has confirmed these parameter ranges [8]. Thus, the estimation algorithm produces reasonable results on an experimental system. Error sources are sensor noise, and soil inhomogeneities caused by non-uniform soil mixing.

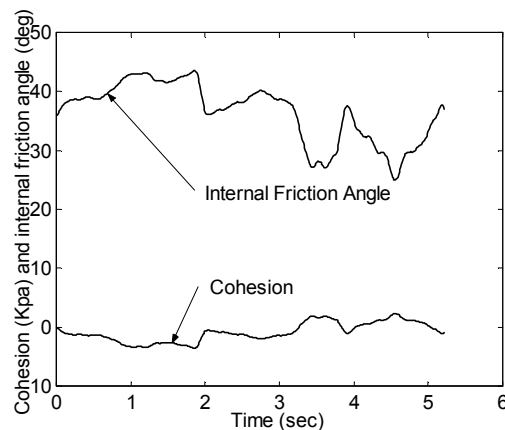


Figure 10: Experimental results of cohesion and internal friction angle estimation

Figure 11 shows a comparison of the measured and predicted drawbar pull for the wheel system. Again, the results are reasonably close.

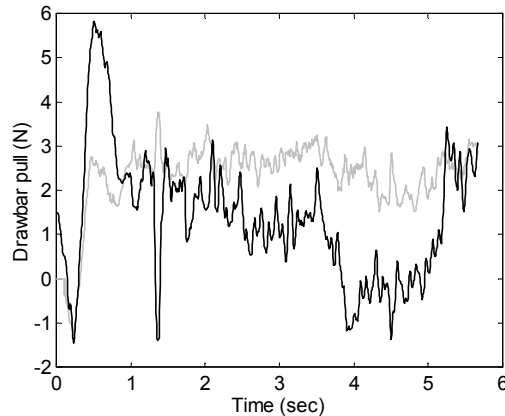


Figure 11: Measured (black) and predicted (gray) *DP*

5. SUMMARY AND CONCLUSIONS

A framework for terrain characterization and identification is briefly described, and an on-line terrain parameter estimation algorithm has been presented. The estimation method is based on simplified forms of classical terramechanics equations. The simplified equations are solved for the cohesion and internal friction angle in real time. Simulation and experimental results show that the estimation method can estimate terrain parameters with good accuracy in the presence of noise, using limited computational resources.

Current work in this area is focused on development of an auditory terrain identification algorithm, and integrating the terrain characterization and identification systems.

ACKNOWLEDGMENTS

This work is currently supported by DARPA and the U.S. Army Tank-Automotive and Armaments Command (TACOM). Previous work in this area, including the terrain estimation research, was sponsored by the NASA Jet Propulsion Laboratory.

REFERENCES

1. Bekker, G., *Theory of Land Locomotion*, University of Michigan Press, 1956
2. Bekker, G., *Introduction to Terrain-Vehicle Systems*, University of Michigan Press, 1969
3. Belluta, P., Manduchi, R., Matthies, L., Owens, K., and Rankin, A., "Terrain Perception for DEMO III," *Proceedings of the 2000 Intelligent Vehicles Conference*, 2000
4. Gerhart, G., Goetz, R., and Gorsich, D., "Intelligent Mobility for Robotic Vehicles in the Army After Next," *Proceedings of the SPIE Conference on Unmanned Ground Vehicle Technology*, Vol. 3693, pp. 128- 139, 1999
5. Hogg, R., Rankin, A., McHenry, M., Helmick, D., Bergh, C., Roumeliotis, S., Matthies, L., "Sensors and Algorithms for Small Robot Leader/Follower Behavior," *Proceedings of the 15th SPIE AeroSense Symposium*, 2001
6. Iagnemma, K., and Dubowsky, S., "Mobile Robot Rough-Terrain Control (RTC) for Planetary Exploration," *Proceedings of the 26th ASME Biennial Mechanisms and Robotics Conference, DETC 2000*, 2000
7. Iagnemma, K., *Rough-Terrain Mobile Robot Planning and Control, with Application to Planetary Exploration*, Ph.D. Thesis, Massachusetts Institute of Technology, Cambridge, MA, 2001

8. Moore, H., Hutton, R., Scott, R., Spitzer, C., and Shorthill, R., "Surface Materials of the Viking Landing Sites, Mars," *Journal of Geophysical Research*, Vol. 82, No. 28, 1977
9. Nohse, Y., Hashiguchi, K., Ueno, M., Shikanai, T., Izumi, H., and Koyama, F., "A Measurement of Basic Mechanical Quantities of Off-The-Road Traveling Performance," *Journal of Terramechanics*, Volume 28, Number 4, pp. 359-371, 1991
10. Onafeko, O., and Reece, A., "Soil Stresses and Deformation Beneath Rigid Wheels", *Journal of Terramechanics*, Vol. 4, Number 1, pp. 59-80, 1967
11. Plackett, C., "A Review of Force Prediction Methods for Off-Road Wheels," *Journal of Agricultural Engineering Research*, Volume 31, pp. 1-29, 1985
12. Schenker, P., *et al.*, "Lightweight Rovers for Mars Science Exploration and Sample Return," *Proceedings of SPIE XVI Intelligent Robots and Computer Vision Conference*, Volume 3208, pp. 24-36, 1997
13. Shmulevich, I., Ronai, D., and Wolf, D., "A New Field Single Wheel Tester," *Journal of Terramechanics*, Volume 33, Number 3, pp. 133-141, 1996
14. Weisbin, C., Rodriguez, G., Schenker, P., Das, H., Hayati, S., Baumgartner, E., Maimone, M., Nesnas, I., and Volpe, R., "Autonomous Rover Technology for Mars Sample Return," *1999 International Symposium on Artificial Intelligence, Robotics and Automation in Space (i-SAIRAS '99)*, 1999
15. Wilcox, B., "Non-Geometric Hazard Detection for a Mars Microrover," *Proceedings of the AIAA Conference on Intelligent Robotics in Field, Factory, Service, and Space*, Volume 2, 1994
16. Wong, J., and Reece, A., "Prediction of Rigid Wheels Performance Based on Analysis of Soil-Wheel Stresses, Part I," *Journal of Terramechanics*, Volume 4, Number 1, pp. 81-98, 1967